Published in final edited form as:

J Phys Chem B. 2023 April 06; 127(13): 2887–2899. doi:10.1021/acs.jpcb.2c07817.

Effect of Cross-seeding of Wild-type Amyloid-b$_{1-40}$ Peptide with Post-translationally Modified Fibrils on Internal Dynamics of the Fibrils Using Deuterium Solid-state NMR

Aryana Rodgers[1], **Matthew Sawaged**[1], **Dmitry Ostrovsky**[2], **Liliya Vugmeyster**[1,*]

[1]Department of Chemistry, University of Colorado Denver, Denver CO USA 80204

[2]Department of Mathematics, University of Colorado Denver, Denver CO USA 80204

Abstract

Post-translationally modified (PTM) amyloid-β (Aβ) species can play an important role in modulating Alzheimer's disease pathology. These relatively lower populated modifications can cross-seed the wild-type Aβ peptides to produce fibrils that retain many structural and functional features of the original PTM variants. We focus on studies of internal flexibility in the cross-seeded Aβ$_{1-40}$ fibrils originating from seeding with two PTM variants with modifications in the disordered N-terminal domain: the ΔE3 truncation and S8-phosphorylation. We employ an array of ^{2}H solid-state NMR techniques, including line shape analysis over a broad temperature range, longitudinal relaxation, and quadrupolar CPMG to assess the dynamics of the cross-seeded fibrils. The focus is placed on selected side-chain sites in the disordered N-terminal domain (G9 and V12), and hydrophobic core methyl and aromatic groups (L17, L34, M35, V36, and F19). We find that many of the essential features of the dynamics present in the original PTM seeds persists in the cross-seeded fibrils, and several of the characteristic features are even enhanced. This is particularly true for the activation energies of the rotameric motions and large-scale rearrangements of the N-terminal domain. Thus, our results on the dynamics complement prior structural and cell toxicities studies suggesting that many PTM Aβ species can aggressively cross-seed the wild-type peptide in a manner that propagates the PTM's signature.

Graphical Abstract

*corresponding author liliya.vugmeyster@ucdenver.edu.

Supporting Information. Supporting Information included with this manuscript is available free of charge via the Internet at http://pubs.acs.org. Figure S1. Additional TEM images. Figure S2-S4. Additional experimental ^{2}H NMR data and fits. Figure S5. Correlation plots.

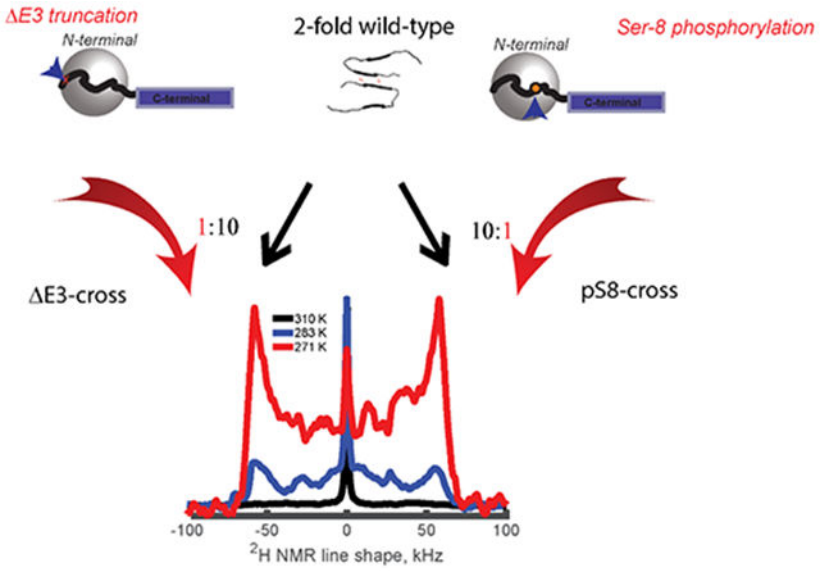

Keywords

Deuterium NMR; solid-state NMR; amyloid-beta fibrils; post-translational modifications

Introduction

Connections between the aggregation states of amyloid-β (Aβ) protein and their relevance to toxicity and eventually Alzheimer's disease (AD) related pathologies remain elusive. Concurrent involvement of other proteins whose aggregation is triggered by toxic Aβ species, such as tau and α-synuclein, was proposed to be important in the amyloid-cascade hypothesis.[1-2] Recently, the role of post-translationally modified Aβ species was highlighted, as many of these modified proteins, especially with the modifications in the disordered N-terminal domain, promote aggressive aggregation pathways and enhanced cellular toxicities, [1, 3-5] thus potentially serving as triggers in the sporadic onset of AD.[4] Among these species are the phosphorylation of serine-8 (pS8) and conversion of glutamate-3 to pyroglutamate via the truncation precursor of the first two N-terminal residues (pyro-E3 and ΔE3, respectively). They were recently characterized by structural, aggregation, and toxicity studies, listed below in more detail. The modifications are located in two different N-terminal domain regions, one closer to the most disordered region (pyro-E3/ΔE3) and the second placed in the middle of the domain (pS8). Because the quantities of PTM's found in the brain tissues of AD patients can be relatively low, it is important to examine how the PTM species influence the aggregates spanned by the wild-type proteins, and in particular whether the cross-seeding of the wild-type Aβ with PTM's retains structural and functional features of the original PTM variants. If this is the case, relatively small quantities of the variants can alter functionality of the wild-type peptide. Prior studies have examined structural and toxicity aspects of these cross-seeding events,[6-7] while here we focus on the internal dynamics features upon cross-seeding (Figure 1). I.e., we ask the question whether the internal flexibility features propagate from the

seeds of post-translationally modified fibrils into the pool of the wild-type $A\beta_{1-40}$ (Figure 1), which is the most abundant form of the Aβ peptide.[8]

Background information on the PTM variants used as seeds

The pS8 $A\beta_{1-40}$ fibrils demonstrated increased nucleation-dependent fibrillation and enhanced Aβ-mediated toxicity in comparison to the wild-type fibrils.[6, 9-10] Structurally, they are similar to the wild-type fibrils in the 2-fold symmetric polymorph.[9] However, the disordered N-terminal domain in these fibrils possess a higher extent of the intra-strand contacts based on solid-state NMR spectroscopy studies.[9] Our previous investigation indicated that the internal dynamics of both the N-terminal and the C-terminal domains are more rigid than those of the wild-type protein, as probed by deuterium solid-state NMR studies.[9, 11] Fibrils cross-seeded *in vitro* with the pS8 modification, have been shown to retain elevated cytotoxicity and contain a more dense intra-strand packing of the N-terminal domain in comparison with the self-seeded fibrils.[6]

The ΔE3 truncation is the first step in the modification pathways along the formation of the pyro-glutamate Aβ variant. It has been shown that both pyro-E3 and ΔE3 Aβ peptides, compared with the wild-type (wt) sequences, lead to a more rapid fibrillation process and results in fibrils with higher neuronal cytotoxicity levels in comparison with the wt fibrils. Cross-seeding with these species also leads to more rapid nucleation-dependent fibrillation kinetics in the wild-type Aβ fibrils and distinctly elevated cytotoxicity compared to the self-seeded fibrils.[6-7, 12] In particular, cellular viabilities were assessed using 3-(4,5-dimethylthiazol- 2-yl)-2,5-diphenyl-tetrazoliumbromide assays in Neuro-2a cells. After 48 hours of incubation different seeds showed comparable toxicity, while the mixture of seeds and monomers showed elevated toxicities, which seemed to stem solely from the cross-seeding events. Compared to the self-seeding, the pyro-E3 and ΔE3 $A\beta_{1-40}$ seeds caused the wild-type Aβ to drop viabilities by a factor of 2.[7] Importantly, the elevation of cellular toxicity levels induced by cross-seeded fibrillization processes was dependent on the type of species. In particular, the presence of pyro-E3- and ΔE3 $A\beta_{40}$ seeds caused more pronounced toxicity increase than the presence of nitrated-Y10 and pS8 seeds, while for the isoD7-seeded fibrillization, the toxicity elevation was comparable to the self-seeding process, as highlighted in Figure 6 of Hu et al.[6]

Further, cross-seeding with the pyroE3/ΔE3-$A\beta_{1-40}$ fibrils lead to significant structural modulations in the resulting fibrils based on ^{13}C solid-state NMR chemical shift and distance restraints, particularly in the N-terminal region.[7] Interestingly, the pyroE3 PTM has been recently identified as an important pharmacological target.[13]

Key features of the dynamics of pS8 and ΔE3 $A\beta_{1-40}$ fibrils

We will now summarize key distinguishing features of dynamics in the pS8 and ΔE3 $A\beta_{1-40}$ variants in comparison with the wild-type fibrils, which we previously determined using ^{2}H solid-state NMR techniques, such as line shape analysis and NMR relaxation studies.[14-16] The fibrils in our investigations are synthetically labeled with site-specific deuterium labels at either methyl groups or phenylalanine rings, with the exception of G9, which is labeled at the backbone (Table 1). Thus, the main motions that we address in the hydrophobic

core regions originate from fast methyl rotations, slower rotameric inter-conversions of the methyl-bearing side-chains, as well as ring flipping motions (Figure 2). In the flexible N-terminal domain, in addition to the above local modes we discern large-scale concerted rearrangements of the domain, including conformational exchange between the free state of the domain and the one transiently interacting with the C-terminal hydrophobic core.

For the structured C-terminal domain, spanning residues approximately 17 to 36, we have found that the pS8 fibrils display an overall rigidifying of the core based on the higher activation barriers of rotameric and ring-flipping motions in the modified fibrils in comparison to the wild-type fibrils.[9] Interestingly, ΔE3 fibrils induce a broader variety of changes, some of which are thermodynamic in nature rather than the kinetic ones, such as modification in the energy differences/populations between the rotameric states.[17] In the N-terminal domain (residues 1-16), the most characteristic motions are those reflecting concerted fluctuations of the domain rather than local modes.[18] Due to transient interactions with the structured C-terminal domain, the N-terminal dynamics is governed by at least two distinct states: the free state in which the domain undergoes collective large-scale fluctuations in diffusion-like manner, and the bound state in which the interactions are quenched due to intra or inter-strand interactions (Figure 2E). Detailed measurements indicated the presence of several free states, or possibly a continuum of multiple free state.[19-20]

The extent of the diffusive motions decreases along the N-terminal sequence, such as from G9 to V12 positions the large scale rearrangements effectively die out in the wild-type fibrils.[18] Additionally, the large scale rearrangements freeze out in sigmoidal fashion with the decrease in temperature, and characterization of the sigmoidal curves and, in particular, the mid-point of the freezing transition serves as parametrization of changes in the dynamics with temperature.[18] The pS8 fibrils displayed increased rigidity at the G9 site, while the ΔE3 variant was observed to have a tendency toward a higher mobility.[11] The temperature dependence of the V12 site was not probed in detail previously in the modified fibrils, and we include its analysis in this work for the PTM's themselves and the cross-seeded fibrils. The V12 site was probed at the physiological temperature for the pS8 modification.[21] As emphasized above, the G9 to V12 region of the N-terminal domain appears to be an important pivotal point for structural differences.[6-7]

Specific goals of the work

The goal of this work is to systematically assess which of these key dynamical features propagate into the cross-seeded wild-type $A\beta_{1-40}$ fibrils. We emphasize that the dynamics in our work pertains to internal flexibility on the structural level in the final state of the fibrils and we do not assess structural/dynamical changes along the pathway from monomers to oligomers to the fibrillar state.

Conservation of the internal dynamics changes in the cross-seeded species implies the possibility that the conformational heterogeneity and interconversions between the states can play a functional role in the cross-seeding events, effectively priming certain conformational substates to drive aggregation and toxicity propensities in the bulk pool of the wild-type Aβ. However, in this work we do not perform any additional toxicities studies for the cross-

seeded fibrils and do not look for any specific correlations between internal flexibility and toxicities. Our results point to different scenarios in regard to internal dynamics achieved by the cross-seeding: some sites display features that are not only conserved but even enhanced in the cross- seeded fibrils, others retain either the wild-type dynamics or intermediate between the wild-type and the PTM fibrils, while for some sites there are differences that go beyond a direct comparison between the wild-type and PTM themselves.

Materials and Methods

Preparation of the fibril samples

The peptides were prepared using solid-state peptide synthesis (Life Technologies Corporation, Carlsbad CA). The amino acids were purchased from Cambridge Isotopes laboratories (Andover, MA) and CDN isotopes (Pointe-Claire, Canada). The peptides were purified by reversed-phase HPLC to the minimal purity level of 95% and their identity and purity were confirmed by mass spectrometry and reversed-phase HPLC. Fibrils were grown following previously developed generation seeding protocols,[11, 22-24] with the deuterium labeled fibrils corresponding to the generation number 4. Briefly, seeded generation growth used a 1:10 molar ratio of seeds, and this was achieved by incubation with gentle 40 rpm orbital agitation for 3–5 days at room temperature at a 0.5 mg/mL peptide concentration in 10 mM of monosodium phosphate buffer (pH 7.4, 0.05% NaN_3). The identity of the seeds (ΔE3 or pS8 peptide) varied depending on the nature of the fibrils desired. The bulk fibrils for the NMR analysis were collected by centrifugal dialysis using Amicon filters with the 3 kDa molecular weight cut-off. Collected fibrils were re-suspended in deionized water, rapidly frozen with liquid nitrogen, and lyophilized. The samples were packed in 5 mm NMR tubes (cut to 21 mm length) using Teflon tape to center the sample volume in the coil of the NMR probe. A hydrated state with a water content of 200% by weight was achieved by pipetting deuterium-depleted H_2O directly in the NMR tubes, followed by flash freezing the hydrated fibrils in the tubes in liquid nitrogen, defrosting, and equilibrating for at least 48 hours to ensure homogeneous hydration.

NMR procedures

Line-shape experiments for the fibrils labeled at one of the G9, V12, L17, L34, M35, and V36 side-chains were performed using a 9.4 T NMR spectrometer equipped with a static Phoenix probe with a 5 mm diameter coil. The quadrupole echo pulse sequence based on an eight-step phase cycle[14] was used, with a delay of 36 μs between 90° pulses. The value of 36 μs was chosen as the minimum time to avoid the probe ringing and maximize the signal. Relaxation delays were set to three times the longitudinal relaxation rates of the methyl deuterons, which were determined by either inversion recovery or saturation recovery experiments. We have previously shown that the relaxation times of the C^{β} and C^{α} deuterons in valine side-chains are much longer than those of methyl deuterons over a wide temperature range and are, thus, saturated in the resulting line shapes within the range of inter-scan delays employed; hence, they do not contribute to the observed signal.[25] Time domain data were left-shifted to the echo maximum and a 500 to 1000 Hz exponential line broadening function was employed. Temperature calibration was carried out by recording the static lead nitrate line shapes.[26]

The ^{2}H T_1 (longitudinal relaxation) measurements for the F19-ring-D_5-labeled fibrils were taken using the 9.4 T spectrometer with the saturation recovery sequence. The multiple-echo (QCPMG) detection scheme was used for signal enhancement[27-28] without the suppression of relaxation anisotropy.[29] Ten QCPMG echoes were collected with 63 μs pulse spacing. The value of the spacing was chosen to provide an adequate signal enhancement without significant heating effects. Eight to nine relaxation delays were collected. ^{2}H QCPMG spectra were processed with 0.2 kHz exponential line broadening.

^{2}H QCPMG-based time-domain transverse relaxation rates measurements at the G9 site were performed as described previously using the multiple-echo acquisition approach.[20] Note that in this case the multiple-echo acquisition was not used for the signal enhancement but rather to obtain the relaxation times themselves. The measurements spanned echo times (τ_{qcpmg}) between 123 and 303 μs with the rf irradiation frequency set exactly on resonance, 15 to 20 echoes were collected, and the restriction in the number of echoes originates from the sample heating effects. The number of scans varied between 4096 and 6144 depending on the signal-to-noise ratio in each sample. The inter-scan delay was set to 0.6 sec and 32 dummy scans were utilized. Integrated echo intensities were fitted to a single-exponential function with no offset.

Modeling

Modeling the line shapes based on the rotameric interconversions (as shown in the models in Figure 2A-C) followed the procedures outlined in detail in prior work.[24, 30-31] The EXPRESS program was used to generate modeled spectra.[32] After accounting for averaging over the fast methyl jumps, the quadrupolar coupling constant was set to C_q=53.3 kHz for V12, L17, L34, and V36 methyl groups and 58 kHz for the M35 methyl groups, with the asymmetry parameter η=0.[31] The fitting parameters of the models, population of the major conformer w, and rotameric exchange rate constant k_{rot} were obtained using the iterative procedure outlined in prior work.[24]

In the line-shape decomposition, the tensorial parameters of the bound state used were C_q=53.3 kHz, η=0 for the V12 methyl sites, which assumes averaging over fast methyl rotations, and C_q=175 kHz kHz, η=0 for the G9 sites.

Modeling the longitudinal relaxation rates for the F19 side-chain, detailed in reference[33-34], involves the creation of relaxation time libraries to obtain the fits of the central value of the log-normal distribution of the k_{flip} rate constant and the widths of the distribution of the constants σ_k, as shown in Figure S6. The parameters of the small-angle fluctuations around the χ_2 angle (Figure 2D) were fixed at the values determined the 2-fold wt fibrils: $\langle E_a^{small} \rangle$ = 10.5 kJ / mol, σ^{small} = 1.7 kJ / mol, and the single Arrhenius prefactor of 2.17 ·10^{10} s^{-1}. The quadrupolar tensor parameters were C_q=180 kHz, η=0. The angles between either the C^{δ}—D or the C^{ε}—D bonds and the C^{β} — C^{γ} axis was taken as 59.2°. The amplitude of the small-angle fluctuations in the 4-site jump model of Figure 2D was taken as $\alpha/2$ = 5°. The errors in the fitted model parameters were determined using the inverse covariance matrix method.

The modeling for Q-CPMG experiment was performed by direct numerical integration of the Liouville–von Neumann equation using the internal MATLAB function for calculating the matrix exponent and only the evolution of the transverse component was considered, while the QCPMG pulses were treated as instantaneous changes in the phase of this component. The powder averaging procedure involving appropriate Euler's angle transformations and the setup of motional frames were taken from the EXPRESS program.[32]

We modeled the conformational exchange matrix K_{ij} according to Figure 2E including the components responsible for the isotropic diffusion and the conformational exchange between the free diffusion state and bound state, with to the following scheme:[16, 18]

$$K = \left(\begin{array}{c|c} \text{diffusion} & \text{exchange with bound state} \\ \hline \text{exchange with bound state} & \end{array} \right)$$

The diffusion state is represented by N_D = 192 discrete sites nearly uniformly distributed over a unit sphere. The diffusion process itself is modelled by the diffusion block of the exchange matrix which is a sparce matrix with non-zero elements given by jump rates between the nearest-neighbor sites (5 to 7 nearest neighbors for any given site). All the non-zero jump rates were taken as equal and the jump rate constant k_D was adjusted to represent the chosen value of diffusion coefficient in the continuous limit. To create the approximately uniform spherical distribution we used the program DistMesh.[35] The inclusion of N_D = 192 sites is sufficient to adequately represent the isotropic diffusion process. The bound state adds one more site and the exchange process corresponds to the jumps between every site describing the spherical diffusion and bound state site with value of the rate constant k_{ex}. The tensor of the free state was taken with the parameters of C_q=77.6 kHz and η=1, which assumes averaging over the fast 2-fold jumps of the - $C^{\alpha}D_2$ group.[18]

Results and Discussion

Preparation of the cross-seeded fibrils.

The monomeric amyloid-β peptides were prepared synthetically with incorporation of specific deuterium isotopic labels (see Table I for the details of the labels). As the result, the fibrils used in this work had a single side-chain labeled either at the disordered N-terminal domain (G9 and V12) or at the structured C-terminal domain (L17, F19, L34, M35, V36). Most of the labels are at the methyl positions, except for the phenylalanine ring of F19 and the backbone of G9. All fibrils were prepared using standard generation seeding protocols, and the details are listed in the Materials and Methods section.[6-7, 10] The fibril seeds to fresh peptide molar ratio was 1:10 and for the case of cross-seeding the seeds consisted of either ΔE3 or pS8 fibrils, while the fresh peptide corresponded to the wild-type $A\beta_{1-40}$. The choice of the ratio of seeds to the monomeric peptide follows the one most thoroughly investigated in the generation seeding approaches literature for the Aβ peptide.[8, 12, 23, 36] The morphologies of each generation were followed with transmission electron microscopy (TEM). Examples of images are shown in Figure 1 and Figure S1. The notation for the cross-seeded fibrils resulting from the ΔE3 variant will be "ΔE3-cross" and those resulting from the pS8 variant will be "pS8-cross". Most of the sites of the PTM variants themselves

were investigated in the previous works,[9, 11, 17] aside from additional data for the V12 site that is included in the manuscript. The comparison with the wild-type fibrils is those in the 2-fold symmetric polymorph,[23, 37] utilizing the same preparation protocols as the PTM and cross-seeded fibrils. For the NMR measurements, the fibrils were hydrated at the lyophilized state via introduction of deuterium depleted water with the 200% by weight water content.

Overview of ^{2}H solid-state NMR approaches and motional modes

^{2}H solid-state NMR is a powerful method for investigation of side-chain dynamics, and we employ a number of techniques to probe the variety of the motional mode characteristic of the side-chains included in this study. [14-16] The hydrophobic core methyl-bearing side chains (L17, L34, M35, and V36) as well as the N-terminal V12 side chain undergo rotameric interconversions that can be investigated by simple line shape analysis techniques, most sensitive to the motions on the order of the quadrupolar coupling interactions. They are around 53-60 kHz after averaging over methyl rotation. The ring-flipping dynamics of the F19 residues is best probed by longitudinal T_1 relaxation measurements, most sensitive to the fluctuations on the order of the Larmor frequency.[33-34]

The N-terminal domain of the fibrils has been shown to undergo large scale motions in the hydrated state, which can be modeled within the two-state exchange model (Figure 2E).[18] The first of these two states corresponds to the so-called “free” state of the N-terminal domain in which these large scale rearrangements are active, while in the second “bound” state the motions are quenched due to interactions with the structured C-terminal domain. The variability of these motions among different PTM and mutants has been especially pronounced around the G9 site.[11] In addition, the G9 and V12 sites were chosen because they served as markers of chemical shift changes in the structural studies of PTM and the cross-seeded fibrils.[7] Thus, we have focused on G9 and V12 sites to investigate the effects of the cross-seeding on the dynamics in the N-terminal domain. The ^{2}H line shape analysis yields the relative fractions of the free and bound states, while the quadrupolar Carr-Purcell-Meiboom-Gill (CPMG) experiment can quantify more precisely the values of the conformational exchange rate constant and the time scale of the large-scale rearrangement of the domain.

Below we will systematically describe NMR results of these measurements and discuss what we learned from the effects of the cross-seeding on the dynamics.

Investigations of rotameric motions by line shape analysis

In the presence of dynamics, the deuterium static solid-state NMR line shapes are modified from the rigid powder patterns and have very distinct shapes (Figure 3). Qualitatively, the internal dynamics narrows the shapes in comparison to the rigid patterns. The most dramatic narrowing at physiological temperature is observed for the N-terminal sites, undergoing large-scale diffusive rearrangements. Rotameric motions usually do not narrow the shapes to the same extent, however they yield very distinct frequency dependent features that reflect the details of the motional modes present and their kinetic and thermodynamic parameters.

The line shape analysis provides information on rotameric populations and rate constants.[15, 38] The number of possible rotamers depend on the number of degrees of freedom (side-chain dihedral angles) and for large number of rotamers an approximation must be used in order to not overfill the data. For the leucine side-chain, in principle, nine rotameric states are possible, however we approximate them within the model of four symmetrical conformers with the tetrahedral geometry (Figure 2A). We justify this simplification by noting that if ideal tetrahedral geometry is used for all dihedral angle orientations, this leads to only four magnetically inequivalent orientations of the methyl axis in the molecular frame, which has proven to be a good approximation in a number of previous studies.[15, 24, 38] Further, we assume one major rotameric state and three identical minor rotameric states, with the relative weights of w:1:1:1. The parameters of the model are thus w and the rotameric rate constant k_{rot}. For the valine side-chain three rotamers are possible with the orientations of the azimuthal angles of 0° and ± 120°. We include all three states with relative weights of w:1:1, corresponding to one major and two equally populated minor states. M35 has the longest side-chain with three dihedral angles with 27 rotameric states theoretically achievable. At temperatures of about 250 K, we have previously shown that it is sufficient to model them with four symmetrical conformers, analogous to the leucine case.[24] Line shapes at each temperature were fitted according to the described models, which yielded the values of k_{rot} and w. The temperature dependence of k_{rot} is taken as Arrhenius, $k_{rot}(T) = k_0 \exp(-E_a / RT)$, and it yields the activation energy E_a of the rotameric motions. The temperature dependence of w follows a Boltzmann-type equation with a possibility of a non-zero intercept for some sites, yielding the energy difference between the energy state designated as ΔE. All of the modeled parameters are defined in Table 2.

A typical example of the temperature dependence of these line shapes are shown in Figure 4(A-D), while examples of fits are shown in Figure 4 (E-H). Additional examples of the experimental data and fits are shown in Figure S2. The parameters E_a and ΔE, obtained with these models using previously described iterative fitting approaches,[24-25] are summarized in Figure 5(A,B), with example of fits in Figure 5(C,D). As there is a potential for correlation between the chosen fitted value of w and k_{rot} at each temperature, for the cross-seeded fibrils we have first attempted to fix the value of w to the value determined for the wt or the corresponding PTM variant, and then vary k_{rot}. This approach has worked well for valine residues with fewer rotameric degrees of freedom, however for leucine residues a good quality fit across all temperatures failed with this approach and the full iterative procedure[24-25] had to be employed.

For the V12 residue, the fraction of the free state had to be separated from the line shape before performing the rotameric modeling. The bound state is the main conformation for this site. We will describe the details of line shape decomposition for determination of the bound and free state fractions in the next section. In the free state, the line shapes are dominated by the overall motions of the domain, rather than the local mode of rotameric inter-conversions.

While the values of E_a report on core packing that govern intern flexibility, it may be of interest to examine whether there is correlation between E_a and the rotameric exchange

constant at the physiological temperature. We did not find any significant trends with the exception of V12, for which the values of k_{rot} at 310 K and E_a appear anti-correlated. For V36 there is a tendency for a positive correlation. (Figure S5).

How do we interpret these parameters in terms of the cross-seeded effects? This is best visualized in the diagrams below for which we color-coded changes in the dynamics on the ribbon-diagram positions separate for the E_a and ΔE parameters (Figure 6).

In Figure 6, shown in red are those sites that display features for which the differences between the PTM and the wild-type fibrils are amplified. This is the case for the increased E_a values at V36, L34, and M35 sites in the pS8-cross fibrils and L17 and M35 side-chains for the ΔE3-cross fibrils. In orange are the sites that are similar to the PTM fibrils, which corresponds to values of ΔE and E_a in V36 residue in the ΔE3-cross fibrils and the value of E_a in V12 for the pS8-cross fibrils. In green there are features that are different from both the wild-type and PTM fibrils.

The most significant observations is that there is a significant number of the sites for which the features of the dynamics characteristic of the PTM fibrils are either conserved or enhanced in the cross-seeded fibrils, which is especially true for the E_a parameters. At the same time, morphologies of resulting cross-seeded species are relatively similar as judged by TEM (Figure 1, S1), thus implying that morphological features do not necessarily correlate with internal flexibility patterns on the microscopic level.

As one of the possible control experiments, we assessed a single site using a different ratio of PTM seeds to the wild-type protein. In particular, we have used 1:50 ratio of ΔE3 seeds to the wt Aβ labeled at the M35 position. Within the precision of the measurements, the resulting line shapes were identical to the ones obtained with the use of seeds in the 1:10 ratio. Morphologies were also very similar as judged by TEM. Additional possibilities to assess the details of the effect of cross-seeding on the dynamics, not performed here, could include cross-seeding a chosen PTM variant with the wild-type seeds, or cross-seeding between different PTM variants.

Investigation of ring-flipping motions of F19 in the hydrophobic core by longitudinal relaxation measurements

The side chain of the F19 undergoes ring-flipping motions that can be sensitive to breathing of the hydrophobic core as a whole unit.[33-34, 39-41] At temperatures below about 270 K the line shapes were found to be no longer sensitive to these motions in the fibrils, and, thus, longitudinal relaxation measurements are more appropriate for probing the activation energy of ring-flipping motions across a wide temperature range.[15, 34] Based on previous results, the dynamics of the F19 side-chain are complex, with ring-flipping motions driving the relaxation at temperatures above 260 K and small-angle fluctuations dominant at lower temperatures.[33] Similar to approaches used for the pS8 and ΔE3 fibrils in prior works,[9, 17] we assumed that the small-angle fluctuations are the same in all the types of fibrils due to their dependence mostly on local structural factors. We, therefore, restricted our measurements to the temperature range above about 250-260 K for probing only the ring-

flipping motions. The small-angle fluctuations were measured in details for the wild-type 2-fold symmetric fibrils.[34]

The multiple echo acquisition detection scheme was employed in the longitudinal T_1 relaxation times measurements,[27] which breaks the powder pattern into a series of spikes, in our case separated by 16 kHz. The spikelet pattern is shown in detail in Figure 7A. The magnetization build-up curves $M(t)$ can then be extracted at the chosen spikelet locations, as the anisotropy is retained in this technique.[29] This is especially important for the detailed analysis of the systems with wide distributions of rate constants, because relaxation in different parts of the spectrum are more sensitive to different parts of the distribution. Figure 7B shows examples of magnetization build-up curves for the ±16 and ±64 kHz spikelets in the ΔE3-cross fibrils. Relaxation is non-exponential and depends strongly on the spikelet frequency, reflecting the heterogeneity of core packing. The build-up curves are fitted by the stretch-exponential function of the form

$$M(t) = M(\infty)(1 - e^{-(t / T_1^{eff})^{\beta}}), \quad (1)$$

in which $M(t)$ is the signal intensity, T_1^{eff} is the effective relaxation time, and β is the parameter that reflects the degree of non-exponentiality, defined in the range of $0 < \beta \leq 1$.[42-43] β less than 1 corresponds to non-exponential behavior. The presence of a significant non-exponentiality, well in excess of what might be expected from a simple orientational dependence, is an indicator of the distribution of the ring-flip constants. The temperature dependence of the extracted parameters is shown in Figure 7C. Apart from the obvious increase in values of T_1^{eff} with the decrease in temperature stemming from the overall slowing of the motions, the details of the temperature dependence of T_1^{eff} and β are complicated and require explicit dynamical modelling to make sense of.

If one assumes that the distribution of the flip rates is the result of the distribution of activation energies E_a^{flip} and that the distribution of the activation energies can be reasonably described as Gaussian with the central value $\langle E_a^{flip} \rangle$ and the width σ^{flip}, then the distribution of ring-flip rate constants at each temperature will be a lognormal distribution with the central value of the rate constant k^{flip} and the width of the lognormal distributions σ_k. Experimental relaxation curves, and in particular their stretched exponential parameters T_1^{eff} and β, can be fitted to the lognormal distribution of relaxation rates which yield the values of the parameters k^{flip} and σ_k at each temperature. Subsequently, the temperature dependence of k^{flip} and σ_k can be fitted to the Arrhenius temperature dependence yielding the values of $\langle E_a^{flip} \rangle$ and σ^{flip}.

The values of T_1^{eff} and β all the temperatures are shown in Figure 7C, while the details of the fits can be found in Figure S3. The resulting values of $\langle E_a^{flip} \rangle$ and σ^{flip} are shown in Figure 7D. The value of $\langle E_a^{flip} \rangle$ in the pS8-cross fibrils is in between the values for the wild-type and the pS8 fibrils, while it is more similar to the PTM itself for the ΔE3-cross fibrils. The value of σ^{flip} in the pS8-cross sample tends to be somewhat smaller than the σ^{flip} in either the wt or pS8 fibrils (although similar within the margins of errors). For the ΔE fibrils the value

of σ^{flip} is significantly smaller compared with the wt fibrils, and this tendency is at least partially retained in the cross seeded fibrils. The results regarding $\langle E_a^{flip} \rangle$ are also included in the color-coded diagram of Figure 6.

Investigation of the disordered N-terminal domain motions at G9 and V12 sites.

In addition to local motional modes, residues in the disordered N-terminal domain of the fibrils have been show to undergo large scale rearrangements according to the two state model described in the Introduction section and illustrated in Figure 2E.[18] The G9 site has proven to be most sensitive to changes in the dynamics among various PTM's variants and mutans,[11] perhaps due to the fact that the large-scale rearrangement start to freeze out at this site and further along the N-terminal sequence at the physiological temperature. The structure of the wild-type fibrils has been reported starting from the residue G9 as well. Additionally, G9 and V12 sites have shown significant structural modulations in the ΔE3 and pyro-E3 fibrils and their corresponding cross-seeded versions based on 2D solid-state ^{13}C NMR chemical shifts.[7]

The two-state motional model of Figure 2E is parametrized by a) the fraction of the bound state p_{bound}, b) the effective diffusion coefficient D for the free state, which yields a phenomenological description of the large-scale rearrangement under the approximation of isotropic diffusion, and c) conformational exchange rate constant between the free and bound state, k_{ex}. The value of p_{bound} is obtained by line shape decomposition, while D and k_{ex} are obtained in the most precise fashion by the relaxation dispersion technique. For G9, the most sensitive technique turned out to be the time domain quadrupolar-CPMG experiment.[44-45] For the V12 residue, the fraction of the free state is very minor and we restrict ourselves to determination of D and k_{ex} only for the most sensitive G9 site.

I. determination of p_{bound} and freezing curves—The line shape decomposition (Figure 4(E-H) and Figure S4) for the V12 sites consists of separating the narrow Lorentzian fraction (free state) and non-Lorentzian fraction (bound state).[18] For G9 the situation is more complex as the non-Lorentzian fraction itself has to be further decomposed into the rigid-like pattern (corresponding to the quadrupolar coupling constant of C_q= 175 kHz and the asymmetry parameter η=0) and the residual component to obtain the fraction of the bound state corresponding to the rigid component. The residual component could stem from deviations from the isotropic diffusion model.[18] The results are summarized in the p_{bound} panel of Figure 8.

At 310 K for the G9 site of ΔE3-cross, the value of p_{bound} (0.28) is the same as for the ΔE3 fibrils (0.26) and different from the wt fibrils (0.36). For pS8-cross fibrils at the G9 site, we observe another example of amplification of differences between the wt and PTM in the corresponding cross-seeded fibrils: the value of p_{bound} in the pS8-cross fibrils (0.63) is significantly higher than that of the pS8 PTM (0.42), which is itself higher than the wt value (0.36). For the V12 site, the values of p_{bound} appear the same within the margins of error for all variants and are in the high range of 0.8 to 0.93. Thus, at this site in which the bound state dominates we no longer observe variability among the variants.

As the temperature is lowered, the fraction of the bound state increases as expected due to freezing of the large-scale motions of the domain (Figure 4 A-D). p_{bound} follows the characteristic sigmoidal shape (Figure 9), which can be fitted to Eq. (2),[18] yielding the midpoint of the freezing curves T_m and the width of the transition σ, summarized in Figure 8. The higher and lower temperature baselines are a and b. The higher value of T_m signifies that the onset of the freezing of the diffusion motions starts at a higher temperature upon sample cooling.

$$p_{bound} = a + \frac{b - a}{1 + \exp\left(\frac{T - T_m}{\sigma}\right)} \quad (2)$$

For the pS8-cross fibrils at 310 K the fraction of the bound state is already at 0.63, thus the freezing curve cannot be parametrized accurately. For ΔE3-cross fibrils, the value of T_m (285 K) is similar to that of the wt fibrils, while the value of σ=2.4 K points to a significantly sharper sigmoidal behavior compared to both the wt (σ=6.2 K) and ΔE3 (σ =8.3 K) fibrils. Thus, while the melting temperature itself is not conserved in the ΔE3-cross fibrils, the sharpness of the curve is enhanced from wt to ΔE3 to ΔE3-cross fibrils.

II. Determination of *D* and k_{ex} in G9 residue by ^{2}H Q-CPMG measurements.—

We have previously determined that for the G9 site in the wild-type, ΔE3 and pS8 fibrils ^{2}H Q-CPMG time domain method provides the best assessment of the conformational exchange process within the two site exchange model of Figure 2E.[11, 20] This model assumes that the there is a single free state which is in the slow exchange with one bound state. The conformational exchange constant was previously determined to be in the range of 2-4·10^4 s^{-1}. The combination of ^{2}H chemical exchange saturation transfer, rotating frame relaxation, and ^{2}H Q-CPMG measurements at several N-terminal domain sites in the wild-type fibrils has shown that the model is a simplification, as there are additional free states which are exchanging with the bound state on different time scales. The major additional state exchanges with an order of magnitude faster rate constant and a different (much faster) diffusion coefficient.[19, 44] However, for the G9 site, for which the fraction of the bound state is significantly higher compared to the more flexible A2-H6 residues, the assumption of the two state model renders a robust qualitative picture of the dynamics without the need of extra parametrization.

The multiple-echo time-domain acquisition scheme yields the refocused echoes pattern, whose intensity is diminished due to the transverse relaxation (T_2) originating from motions (Figure 10). By varying the time between the echoes (τ_{QCPMG}) one obtains characteristic dispersion profiles (Figure 10B), i.e. T_2 as a function of τ_{QCPMG}, which can be fitted to the model such as Figure 2E to obtain motional parameters. The experimental values of τ_{QCPMG} were governed by the time scales of motions, with the sensitivity range optimized in prior work.[18]

The fitting parameters are the diffusion coefficient of the free state *D*, the conformational exchange rate constant k_{ex} and p_{bound}. In practice, we found that fixing the value of p_{bound} from

that obtained on the basis of the line-shape analysis simplifies the search grid for D and k_{ex} without compromising the accuracy of the results.

A practical limitation of the Q-CPMG approach is that for wide powder patterns, such as the bound state of G9 with the quadrupolar tensor coupling constant of 175 kHz, the probe ringing effects can be significant. This can be observed in the flat profiles of the individual echoes in Figure 10A, as opposed to the ideal *sinc* function, indicating that the wider components of the powder pattern are cut-off. Thus, for the pS8-cross sample with the large value of p_{bound} we could not obtain accurate results.

We thus limited our measurements to the ΔE3-cross fibrils and compared them with the prior data on the wt and ΔE3 fibrils. The resulting values of D and k_{ex} are shown in Figure 10. As can be seen from the dispersion profiles themselves (Figure 10B), the behavior displayed by the ΔE3-cross fibrils is identical to the ΔE3 fibrils, with the value of $D = 3 \cdot 10^5$ rad^2/s and the value of k_{ex} of $4.5 \cdot 10^4$ s^{-1},[11] which is about a factor of two higher than the value of k_{ex} in the wt fibrils. The value of D is the same in all three types of fibrils. Thus, the parameters of the two-state model are identical between the ΔE3 and ΔE3-cross fibrils and are somewhat different than those for the wt fibrils.

Conclusions

Based on the detailed ^{2}H solid-state NMR and modeling analysis of selected N-terminal and hydrophobic core residues in the ΔE3 and pS8 cross-seeded fibrils, we conclude that cross-seeding the wild-type A$\beta_{1\text{-}40}$ peptide with these PTM seeds leads to fibrils that appear to conserve or even enhance many dynamical features characteristic of the original post-translationally modified fibrils. This is especially apparent for the activation energies of rotameric motions of the hydrophobic core methyl groups and the N-terminal domain large-scale rearrangements that include conformational exchange between the domains, as probed at the critical G9 site. Other features show more variability in terms of their propagation into the cross-seeded fibrils, such as the energy differences of the rotameric states, with some sites displaying parameters not similar to either the self-seeded wt or the PTM fibrils. Combined with prior structural and functional studies of the PTM and cross-seeded fibrils described in the Introduction, it is clear that cross-seeding of the wild-type Aβ can lead to structural, dynamics, and functional features that are very different from the self-seeded fibrils and can cause the resulting modified structural landscape to become more prone to aggregation. It is possible that the conformational selection mechanism[46-47] might be in place for these cross-seeding events in both *in vivo* and *in vitro* situations. The role of specific interactions in amyloid growth and propagation has been recently highlighted in computational and experimental works.[48-50] Thus, when PTM's are present even in relatively small amounts, they can impose their functionality on the wild-type Aβ peptides and it is important to include the whole subset of the wild-type, post-translationally modified, and cross-seeded fibrils into the analysis of structure-function relation. Our results can be useful in clarifying major factors acting in the cross-seeding mechanism of various amyloids.

Supplementary Material

Refer to Web version on PubMed Central for supplementary material.

Acknowledgements:

this work has been supported by National Institutes of Health (NIH) Grant 1R15-GM111681 to L.V.

References

1. Barykin EP; Mitkevich VA; Kozin SA; Makarov AA, Amyloid β modification: a key to the sporadic Alzheimer's Disease? Front. Genet 2017, 8, 58–58. [PubMed: 28555154]
2. Musiek ES; Holtzman DM, Three dimensions of the amyloid hypothesis: time, space and 'wingmen'. Natur. Neurosci 2015,18 (6), 800–806. [PubMed: 26007213]
3. Roher AE; Kokjohn TA; Clarke SG; Sierks MR; Maarouf CL; Serrano GE; Sabbagh MS; Beach TG, APP/Aβ structural diversity and Alzheimer's disease pathogenesis. Neurochem. Int 2017, 110, 1–13. [PubMed: 28811267]
4. Kummer MP; Heneka MT, Truncated and modified amyloid-beta species. Alzheim. Reser. Ther 2014, 6 (3).
5. Ke PC; Zhou R; Serpell LC; Riek R; Knowles TPJ; Lashuel HA; Gazit E; Hamley IW; Davis TP; Fändrich M, et al. , Half a century of amyloids: past, present and future. Chem. Soc. Rev 2020, 49 (15), 5473–5509. [PubMed: 32632432]
6. Hu Z-W; Au DF; Cruceta L; Vugmeyster L; Qiang W, The N-terminal modified Aβ variants enable modulations to the structures and cytotoxicity levels of wild-type Aβ fibrils through cross-seeding. ACS Chem. Neurosci 2020, 11, 2058–2065. [PubMed: 32603584]
7. Hu ZW; Cruceta L; Zhang S; Sun Y; Qiang W, Cross-seeded fibrillation induced by pyroglutamate-3 and truncated Aβ(40) variants leads to Aβ(40) structural polymorphism modulation and elevated yoxicity. ACS Chem. Neurosci 2021, 12 (19), 3625–3637. [PubMed: 34524791]
8. Pauwels K; Williams TL; Morris KL; Jonckheere W; Vandersteen A; Kelly G; Schymkowitz J; Rousseau F; Pastore A; Serpell LC, et al. , Structural basis for increased toxicity of pathological Aβ42:Aβ40 ratios in Alzheimer disease. J. Biol. Chem 2012, 287 (8), 5650–5660. [PubMed: 22157754]
9. Hu ZW; Vugmeyster L; Au DF; Ostrovsky D; Sun Y; Qiang W, The Molecular structure of a “seeding-prone” N-terminal phosphorylated b-amyloid fibril. Proc. Natl. Acad. Sci. U.S.A 2019, 116, 11253–11258. [PubMed: 31097588]
10. Hu Z-W; Ma M-R; Chen Y-X; Zhao Y-F; Qiang W; Li Y-M, Phosphorylation at Ser8 as an intrinsic regulatory switch to regulate the morphologies and structures of Alzheimer's 40-residue β-amyloid (Aβ40) fibrils. J. Biol. Chem 2017, 292 (7), 2611–2623. [PubMed: 28031462]
11. Vugmeyster L; Au DF; Ostrovsky D; Kierl B; Fu R; Hu ZW; Qiang W, Effect of post-translational modifications and mutations on amyloid-beta fibrils dynamics at N Terminus. Biophys J 2019, 117 (8), 1524–1535. [PubMed: 31570231]
12. Wulff M; Baumann M; Thummler A; Yadav JK; Heinrich L; Knupfer U; Schlenzig D; Schierhorn A; Rahfeld JU; Horn U, et al. , Enhanced fibril fragmentation of N-terminally truncated and pyroglutamyl-modified Abeta peptides. Angew. Chem. Int. Ed 2016, 55 (16), 5081–4.
13. Bayer TA, Pyroglutamate Aβ cascade as drug target in Alzheimer's disease. Mol. Psychiatry 2022,27 (4), 1880–1885. [PubMed: 34880449]
14. Void RL; Void RR, Deuterium Relaxation in Molecular Solids. In Advances in Magnetic and Optical Resonance, Warren W, Ed. Academic Press: San Diego, 1991; Vol. 16, pp 85–171.
15. Vugmeyster L; Ostrovsky D, Static solid-state 2H NMR methods in studies of protein side-chain dynamics. Prog. Nucl. Magn. Reson. Spec 2017, 101, 1–17.
16. Vugmeyster L, Recent developments in deuterium solid-state NMR for the detection of slow motions in proteins. Solid State Nucl. Magn. Reson 2021, 111, 101710. [PubMed: 33450712]

17. Vugmeyster L; Fai Au D; Smith MC; Ostrovsky D, Comparative hydrophobic core dynamics between wild-type amyloid-β fibrils, Glutamate-3 truncation, and Serine-8 phosphorylation. ChemPhysChem. 2021, 23, e202100709. [PubMed: 34837296]

18. Au DF; Ostrovsky D; Fu R; Vugmeyster L, Solid-state NMR reveals a comprehensive view of the dynamics of the flexible, disordered N-terminal domain of amyloid-β fibrils. J. Biol. Chem 2019, 294, 5840–5853. [PubMed: 30737281]

19. Vugmeyster L; Ostrovsky D; Fu R, Deuteron quadrupolar chemical exchange saturation transfer (Q-CEST) solid-State NMR for static powder samples: approach and applications to amyloid-β Fibrils. ChemPhysChem. 2020, 21, 220–231. [PubMed: 31805217]

20. Vugmeyster L; Au DF; Ostrovsky D; Fu R, Deuteron solid-state NMR relaxation measurements reveal two distinct onformational exchange processes in the disordered N-terminal domain of amyloid-b fibrils. ChemPhysChem. 2019, 20, 1680. [PubMed: 31087613]

21. Vugmeyster L; Ostrovsky D, Deuterium solid-state NMR quadrupolar order rotating frame method with applications to amyloid-b fibrils. Magn. Reson. Chem 2020, (59), 853–863. [PubMed: 33161607]

22. Xiao Y; Ma B; McElheny D; Parthasarathy S; Long F; Hoshi M; Nussinov R; Ishii Y, Abeta(1-42) fibril structure illuminates self-recognition and replication of amyloid in Alzheimer's disease. Nat Struct Mol Biol 2015, 22 (6), 499–505. [PubMed: 25938662]

23. Petkova AT; Leapman RD; Guo ZH; Yau WM; Mattson MP; Tycko R, Self-propagating, molecular-level polymorphism in Alzheimer's beta-amyloid fibrils. Science 2005, 307 (5707), 262–265. [PubMed: 15653506]

24. Vugmeyster L; Clark MA; Falconer BI; Ostrovsky D; Gantz D; Qiang W; Hoatson GL, Flexibility and solvation of amyloid -beta hydrophobic core. J. Biol. Chem 2016, 291, 18484–95. [PubMed: 27402826]

25. Vugmeyster L; Ostrovsky D; Khadjinova A; Ellden J; Hoatson GL; Void RL, Slow motions in the hydrophobic core of chicken villin headpiece subdomain and their contributions to configurational entropy and heat capacity from solid-state deuteron NMR measurements. Biochemistry 2011, 50 (49), 10637–10646. [PubMed: 22085262]

26. Beckmann PA; Dybowski C, A thermometer for nonspinning solid-state NMR spectroscopy. J. Magn. Reson 2000, 146 (2), 379–380. [PubMed: 11001855]

27. Larsen FH; Jakobsen HJ; Ellis PD; Nielsen NC, High-field QCPMG-MAS NMR of half-integer quadrupolar nuclei with large quadrupole couplings. Mol. Phys 1998, 95 (6), 1185–1195.

28. Larsen FH; Jakobsen HJ; Ellis PD; Nielsen NC, Sensitivity-enhanced quadrupolar-echo NMR of half-integer quadrupolar nuclei. Magnitudes and relative orientation of chemical shielding and quadrupolar coupling tensors. J. Phys. Chem. A 1997, 101 (46), 8597–8606.

29. Vold RL; Hoatson GL; Vugmeyster L; Ostrovsky D; De Castro PJ, Solid state deuterc relaxation time anisotropy measured with multiple echo acquisition. Phys. Chem. Chem. Phys 2009, 11 (32), 7008–7012. [PubMed: 19652835]

30. Vugmeyster L; Ostrovsky D, Temperature dependence of fast carbonyl backbone dynamics in chicken villin headpiece subdomain. J. Biomol. NMR 2011, 50 (2), 119–127. [PubMed: 21416162]

31. Vugmeyster L; Ostrovsky D; Ford JJ; B. SD; Lipton AS; Hoatson GL; Vold RL, Probing the dynamics of a protein hydrophobic core by deuteron solid-state nuclear magnetic resonance spectroscopy. J. Am. Chem. Soc 2009,131 (38), 13651–13658. [PubMed: 19772361]

32. Vold RL; Hoatson GL, Effects of jump dynamics on solid state nuclear magnetic resonance line shapes and spin relaxation times. J. Magn. Reson 2009, 198 (1), 57–72. [PubMed: 19201232]

33. Vugmeyster L; Ostrovsky D; Hoatson GL; Qiang W; Falconer BI, Phenylalanine side-chain in the hydrophobic core of amyloid fibrils reveals a solvent-driven dynamical transition. J. Phys. Chem. B 2017, 121 (30), 7267–7275. [PubMed: 28699757]

34. Vugmeyster L; Osrovsky D; Villafranca TR; Sharp J; Xu W; Lipton AS; Hoatson GL; Vold RL, Dynamics of hydrophobic core phenylalanine residues probed by solid-state deuteron NMR. J. Phys. Chem. B 2015, 119, 14892–14904. [PubMed: 26529128]

35. Persson P-O; Strang G, A Simple mesh generator in MATLAB. SIAM Rev. 2004, 46 (2), 329–345.

36. Paravastu AK; Leapman RD; Yau WM; Tycko R, Molecular structural basis for polymorphism in Alzheimer's beta-amyloid fibrils. Proc. Natl. Aca. Sci. U.S.A 2008, 105 (47), 18349–18354.
37. Petkova AT; Yau WM; Tycko R, Experimental constraints on quaternary structure in Alzheimer's beta-amyloid fibrils. Biochemistry 2006, 45 (2), 498–512. [PubMed: 16401079]
38. Vugmeyster L; Ostrovsky D, Basic Experiments in 2H static NMR for the characterization of protein side-chain dynamics. Methods 2018, 148, 136–145. [PubMed: 29705208]
39. Wagner G; Demarco A; Wuthrich K, Dynamics of aromatic amino acids residues in globular conformation of Basic Pancreatic Trypsin inhibitor(BPTI). 1. H-1 NMR-studies. Biohys. Struct. Mech 1976, 2 (2), 139–158.
40. Hattori M; Li H; Yamada H; Akasaka K; Hengstenberg W; Gronwald W; Kalbitzer HR, Infrequent cavity-forming fluctuations in HPr from Staphylococcus carnosus revealed by pressure- and temperature-dependent tyrosine ring flips. Prot. Sci 2004, 13 (12), 3104–3114.
41. Mariño Pérez L; Ielasi FS; Bessa LM; Maurin D; Kragelj J; Blackledge M; Salvi N; Bouvignies G; Palencia A; Jensen MR, Visualizing protein breathing motions associated with aromatic ring flipping. Nature 2022, 602 (7898), 695–700. [PubMed: 35173330]
42. Sillescu H, Heterogeneity at the glass transition: a review. J. NonCryst. Sol 1999, 243 (2-3), 81–108.
43. Vugmeyster L; Ostrovsky D; Penland K; Hoatson GL; Vold RL, Glassy dynamics of protein methyl groups revealed by deuteron NMR. J. Phys. Chem. B 2013, 117 (4), 1051–1061. [PubMed: 23301823]
44. Vugmeyster L; Ostrovsky D, Deuterium rotating frame NMR felaxation measurements in the solid state under static conditions for quantification of dynamics. Chemphyschem. 2019, 20, 333–342. [PubMed: 30079456]
45. Larsen FH; Jakobsen HJ; Ellis PD; Nielsen NC, Molecular dynamics from 2H quadrupolar Carr–Purcell–Meiboom–Gill solid-state NMR spectroscopy. Chem. Phys. Lett 1998, 292 (4), 467–473.
46. Ma B; Kumar S; Tsai C-J; Nussinov R, Folding funnels and binding mechanisms. Protein Eng. Des. Sel 1999, 12 (9), 713–720.
47. Boehr DD; Nussinov R; Wright PE, The role of dynamic conformational ensembles in biomolecular recognition. Nat. Chem. Biol 2009, 5 (11), 789–796. [PubMed: 19841628]
48. Chang H-W; Ma H-I; Wu Y-S; Lee M-C; Chung-Yueh Yuan E; Huang S-J; Cheng YS; Wu M-H; Tu L-H; Chan JCC, Site specific NMR characterization of abeta-40 oligomers cross seeded by abeta-42 oligomers. Chem. Sci 2022, 13 (29), 8526–8535. [PubMed: 35974768]
49. Koloteva-Levine N; Aubrey LD; Marchante R; Purton TJ; Hiscock JR; Tuite MF; Xue W-F, Amyloid particles facilitate surface-catalyzed cross-seeding by acting as promiscuous nanoparticles. Proc. Natl. Acad. Sci. U S A 2021, 118 (36), e2104148118. [PubMed: 34462352]
50. Ma B; Nussinov R, Selective Molecular recognition in amyloid growth and transmission and cross-species barriers. J. Mol. Biol 2012, 421 (2), 172–184. [PubMed: 22119878]

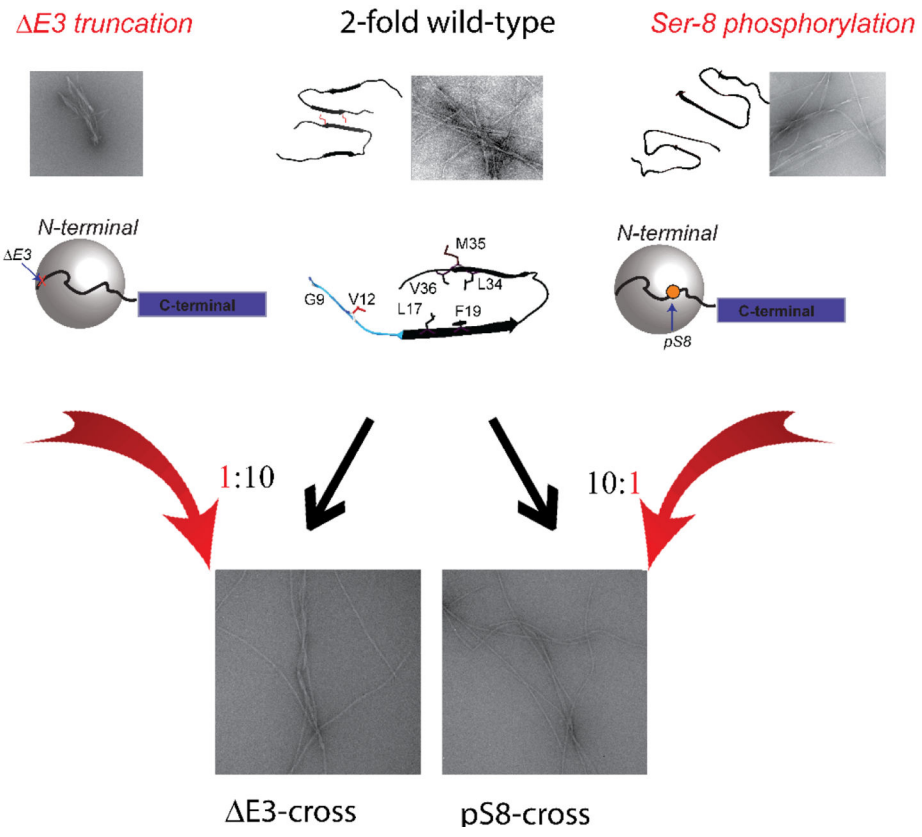

Figure 1.

Demonstration of cross-seeding processes between the PTM fibrils (either the ΔE3 truncation or Ser-8 phosphorylation) and the wild-type $A\beta_{1\text{-}40}$, with the seeds utilized in 1:10 molar ratio. Also shown are typical images of the wild-type $A\beta_{1\text{-}40}$ fibrils in the 2-fold symmetric polymorph, PTM fibrils, and of the resulting cross-seeded fibrils. The quaternary structures of the 2-fold wt $A\beta_{1\text{-}40}$ (PDB ID 2LMN)[23, 37] and pS8 fibrils (PDB ID 6OC9)[9] are shown next to the TEM images. The middle row demonstrates the ribbon diagram of the monomeric Aβ fibrils with the side-chain probed in this work explicitly labeled. The middle row demonstrates the flexible disordered N-terminal domain (residues 1-16), shown as a sphere and the structured hydrophobic core (shown as a blue rectangle), with the sites of the two PTM indicated by the orange dots.

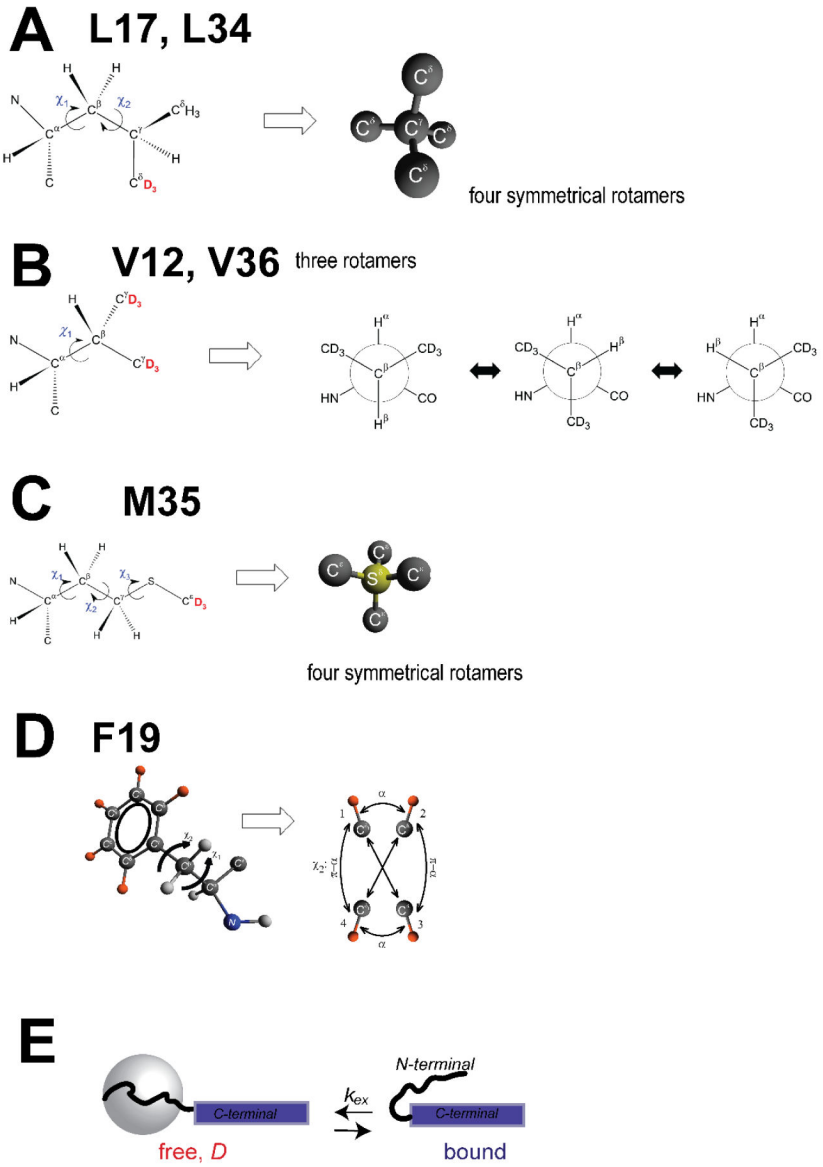

Figure 2.

Motional models[18, 24, 33] for local motional modes of A) L17, L34: rotameric jumps around the χ_1 and χ_2 angles are represented by four magnetically non-equivalent conformers (out of the nine possible configurations), pointing toward the corners of a tetrahedron. The positions of the ^{2}H labels at the methyl groups of the side-chains are shown in red. B) V12 and V36: rotameric jumps around the χ_1 angle are represented by three conformers, g^+, t, and g^-. C) M35: rotameric jumps (involving, in reality, all three χ_1, χ_2, and χ_3 angles) are approximated by four artificial symmetrical conformers with the tetrahedral geometry. D) F19: aromatic ring-flips and small-angle fluctuations around the χ_2 dihedral angle in the phenylalanine side-chains. Left panel: The phenylalanine side-chain with the deuteron-labeling pattern marked in orange. The diagram to the right displays the sites' connectivities according to the 4-site strong collision model, illustrated for one of the C^δ—D bonds. The large-angle aromatic flips occur between sites 1–3 and 1–4 with an

equal probability; this also holds for the 2–3 and 2–4 pairs. The small-angle jumps with the amplitude α=5° occur between sites 1–2 and 3–4. E) Schematic representation of the model of concerted fluctuations of the N-terminal domain residues G9 and V12: the disordered N-terminal domain (curved line) transiently interacts with the structured C-terminal domain (blue rectangle). In the free state, the N-terminal domain is assumed to undergo isotropic diffusion, as represented by the gray sphere, while in the bound state, the interactions quench this mode. The parameters of the models are shown as the corresponding symbols.

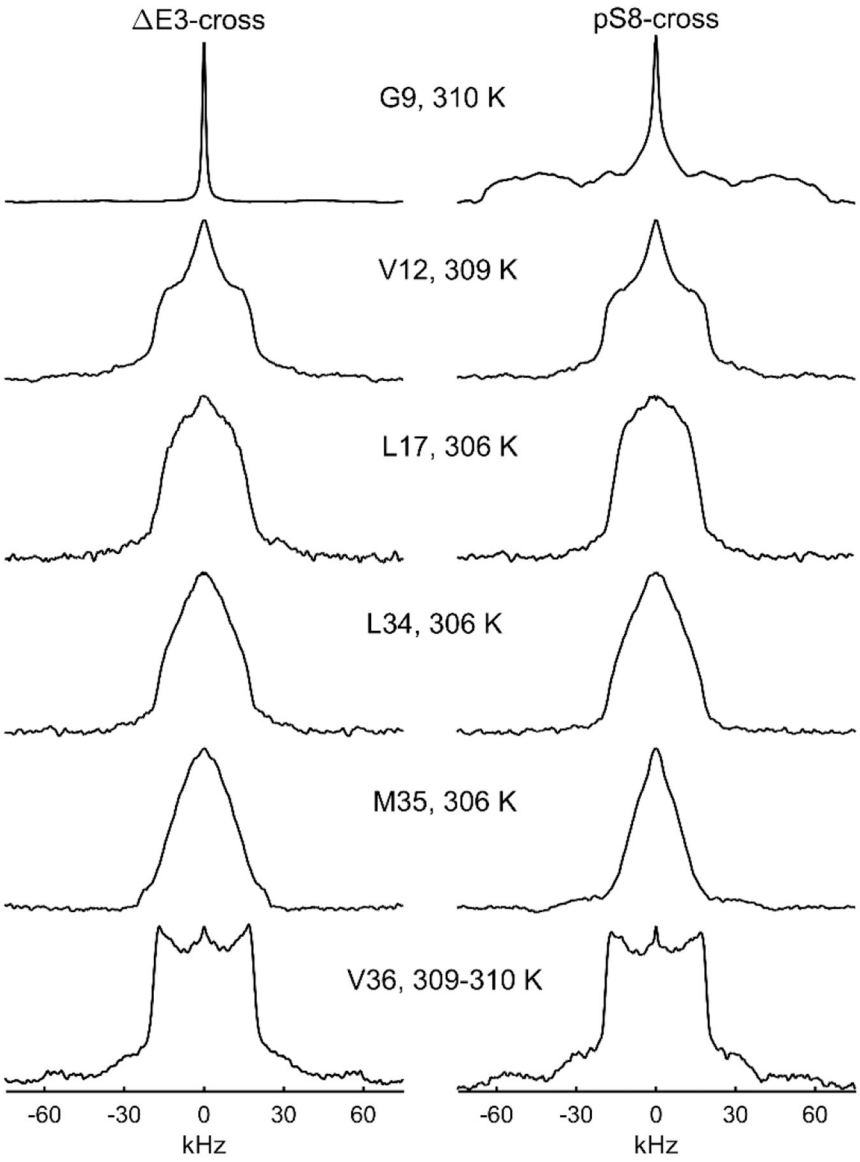

Figure 3.

Representative ^{2}H solid-state NMR line shapes at the temperature close to the physiological for different sites of the ΔE3-cross and pS8-cross fibrils. The line shapes were recorded at 9.4 T using the quadrupolar echo pulse sequence.

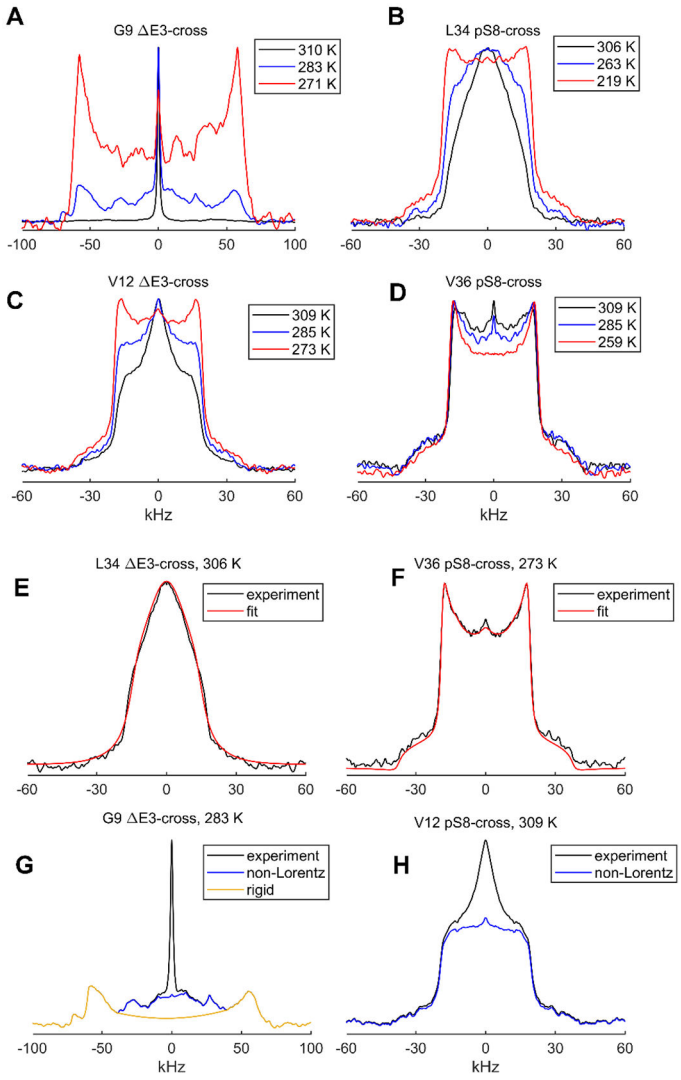

Figure 4.

A-D) Representative experimental ^{2}H solid-state NMR line shapes at different temperatures normalized to major singularities of the powder patterns. E-F) Examples of ^{2}H NMR spectra line shape analysis. Fit of the normalized experimental spectra (black) to the rotameric exchange model (red) with four rotamers in *w*:1:1:1 populations ratio for the L34 site (**E**) and three rotamers in *w*:1:1 populations ratio for the V36 site (**F**). Line shape decomposition of normalized experimental spectra (black) at the G9 (**G**) and V12 (**H**) sites, via decomposition into the non-Lorentz contribution (blue for V12, blue overlapping with yellow for G9) and the rigid compound (yellow) for the case of G9. The types of sites and fibrils are shown directly on the panels.

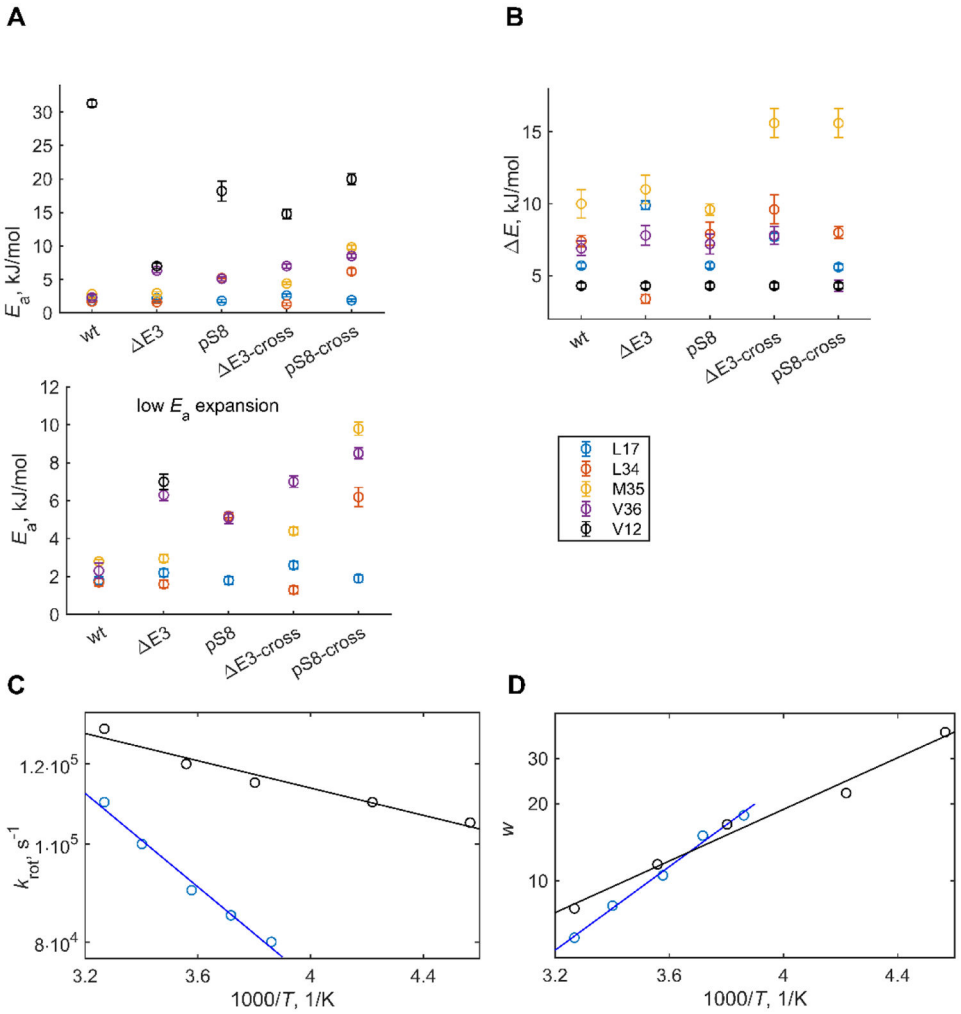

Figure 5.

A) Activation energies of the rotameric inter-conversions E_a, with the low range expansion shown in the bottom panel. B) Energy differences between the major and minor rotameric states Delta$E$ for different types of fibrils and different types of sites. The bottom panel shows the low range expansion of E_a values. Examples of modeled parameters' fits demonstrated for the ΔE3-cross fibrils for the side-chains of M35 (blue circles) and L34 (black circles): rotameric exchange rates, k_{rot} vs $1000/T$(C) and w vs $1000/T$(D), on semilog scales. The lines represent linear fits to the data.

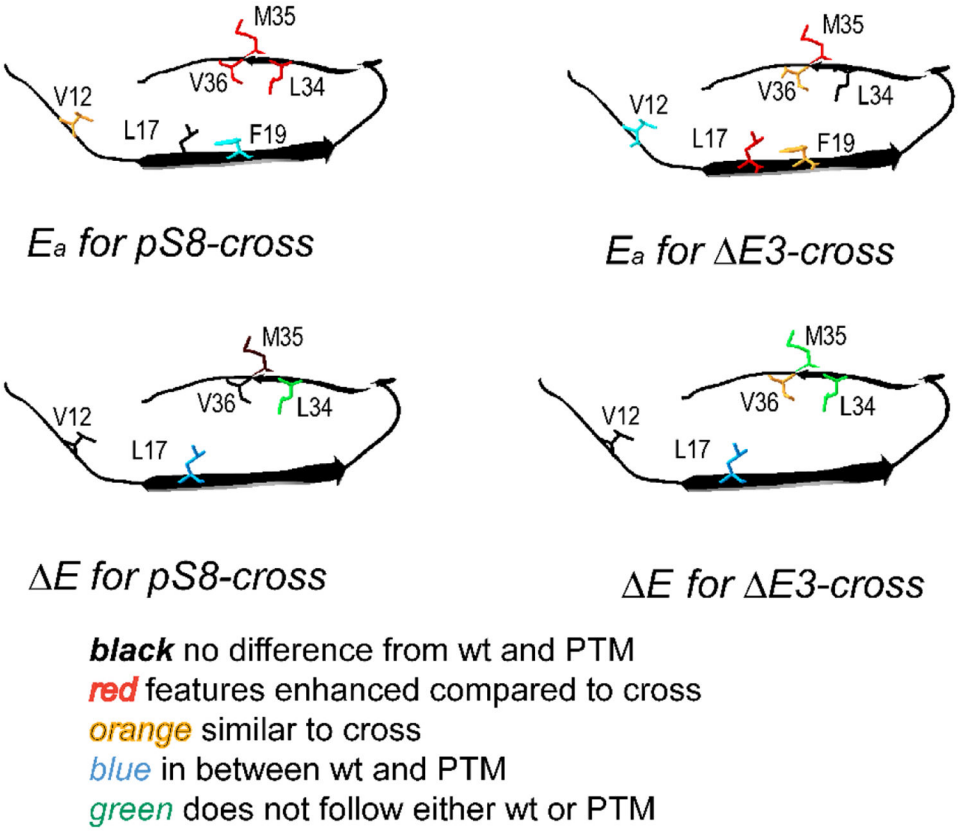

Figure 6.

Schematic diagram indicating comparisons of E_a and Delta$E$ values between the wild-type, PTM, and the cross-seeded fibrils. The side-chains, shown on the ribbon diagram of the monomer (PDB ID 2LMN), are color-coded according to their relative values of E_a (upper row) and Delta$E$ (bottom row). The values of $\langle E_a^{flip} \rangle$ for F19 ring-flipping motion is also included in the upper panel. The color coding is shown directly on the figure.

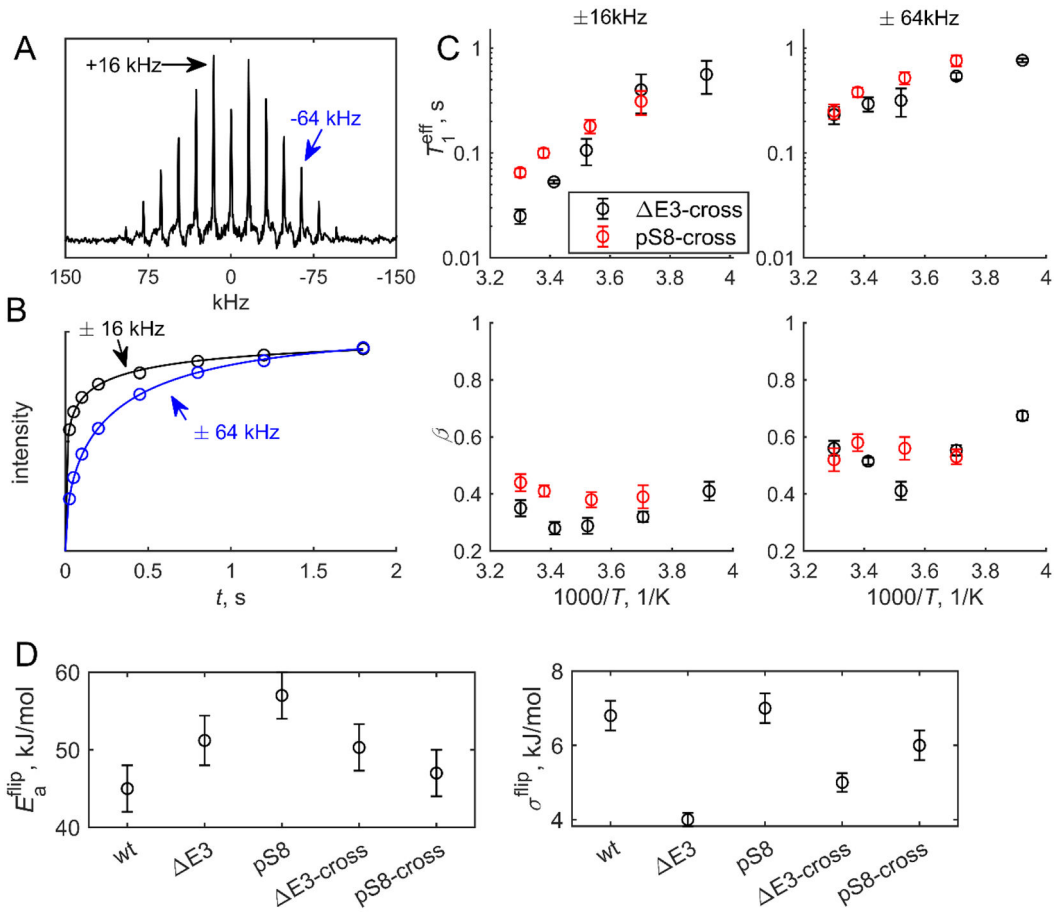

Figure 7.

^{2}H static NMR longitudinal relaxation measurement data for the F19-ring-D5 sites, collected at 9.4 T. A) An example of spectrum collected with the multiple-echo acquisition scheme,[28-29] shown for ΔE3-cross fibrils at 293 K, demonstrating the spikelet pattern spaced at 16 kHz intervals. B) Normalized magnetization build-up curves for the spikelets at ±16 kHz (blue) and ±64 kHz (black) for the ΔE3 fibrils at 293 K, resulting from the saturation recovery measurements. The lines represent the fits to the stretched exponential function of Eq.(1). C) T_1^{eff} and β versus $1000/T$ for the ΔE3-cross (black circles) and pS8-cross (red circles) fibrils at the ±16 kHz and ±64 kHz spikelets. D) Fitted parameters of the $\langle E_a^{flip} \rangle$ (left) and σ^{flip} (right) for different types of fibrils at the F19-ring-D_5 sites.

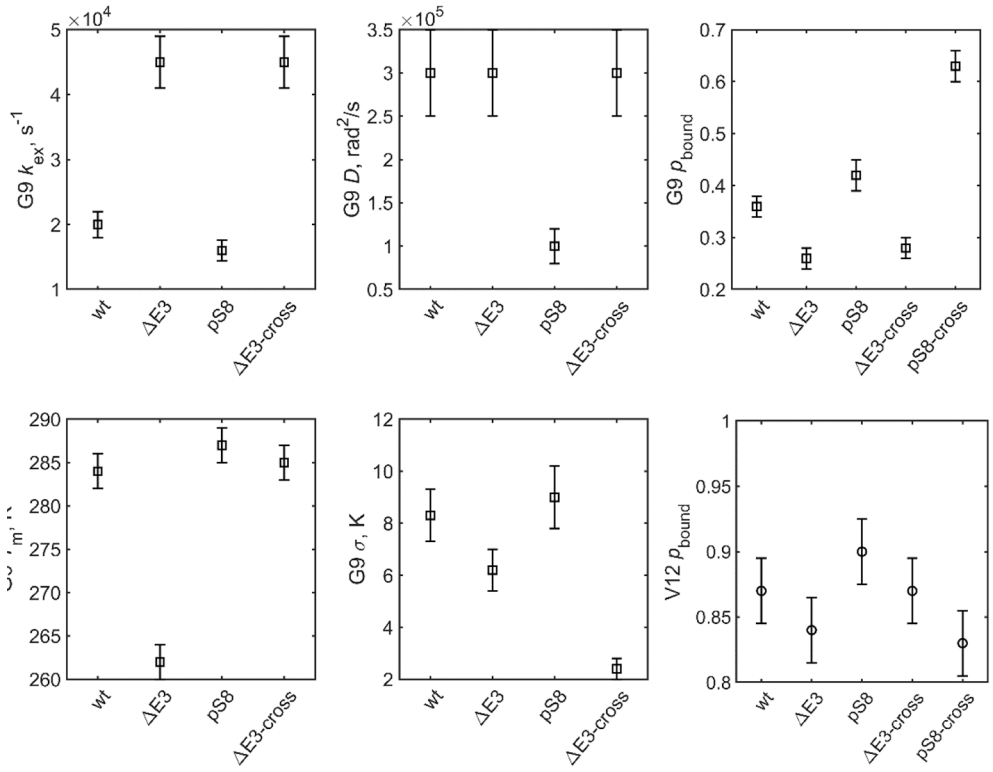

Figure 8.

Summary of the modeled parameters, as indicated on the y-axis of each plot for different types of fibrils. For the V12 sites only p_{bound} at 310 K is shown. For the G9 sites the following parameters are shown: p_{bound} at 310 K, T_m, D. k_{ex}, σ, excluding pS8-cross residue for which only p_{bound} at 310 K was determined.

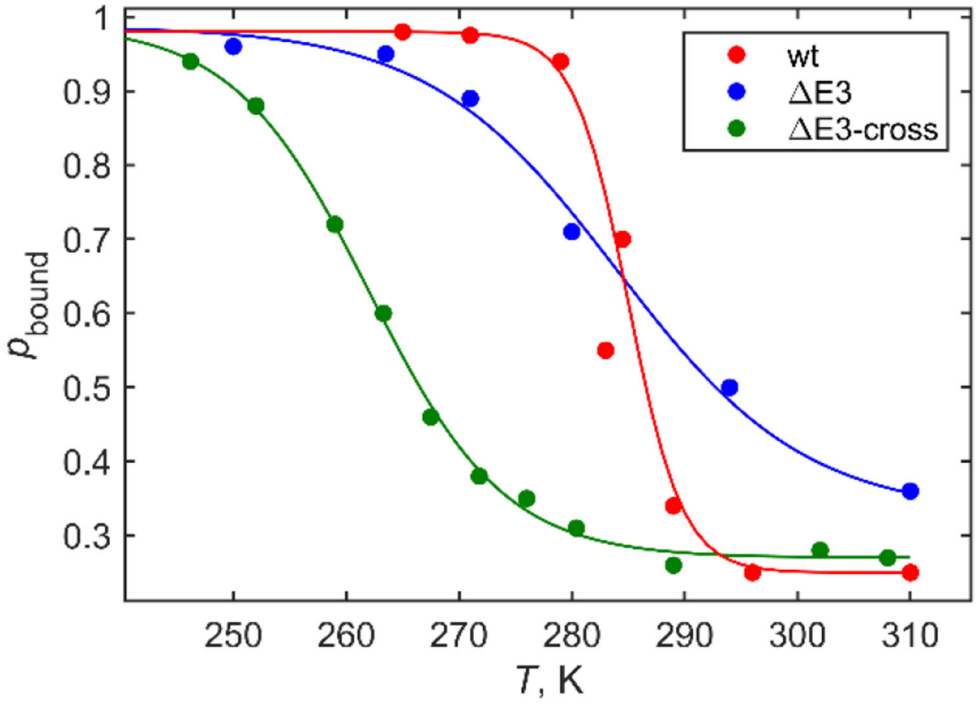

Figure 9.

Freezing curves corresponding to plots of p_{bound} vs T, for the wt (red circles), ΔE(blue circles), and ΔE3-cross (green circles) fibrils. The lines correspond to the fits to Eq. (2).

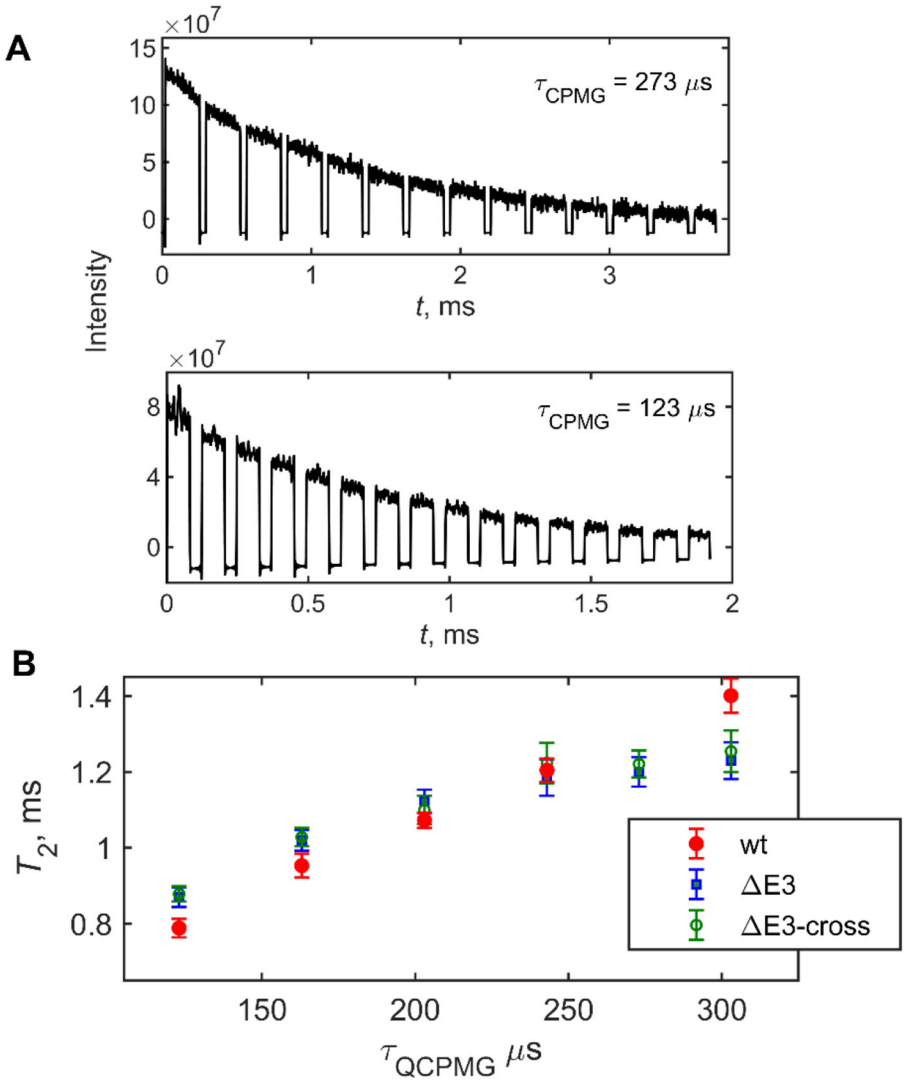

Figure 10.

A) Examples of the multiple-echo (^{2}H Q-CPMG) time domain data for the ΔE3-cross fibrils at the G9 site, with the values of τ_{QCPMG} (the time between the echoes) shown directly on the panels. Intensities in arbitrary units are plotted as a function of time. B) T_2 times versus τ_{QCPMG} for the G9 site in the three types of fibrils wt (red circles), ΔE3 (blue circles), and ΔE3-cross (green circles). The data for the latter fibrils were taken at 9.4 T at 310 K, while the prior results[11, 20] on the ΔE3 and wt fibrils were collected at 14.1 T at the same temperature.

Table 1.

^{2}H labeling patterns and main motional modes present in residues used in this work.

Residues	Most important dynamics mode	^{2}H labeling pattern
G9	Overall diffusive motion of the N-terminal domain	C^{α}-D_2
V12	Overall diffusive motion of the N-terminal domain, rotameric interconversions	C^{β}-D_2-C^{γ}-D_3
L17, L34	Rotameric interconversions	C^{δ}-D_3
M35	Rotameric interconversions, smaller-angle methyl axis motions	C^{ϵ}-D_3
V36	Rotameric interconversions	C^{β}-D_2-Cγ-D_3
F19	Ring-flipping motions	Ring-D_5

Table 2.

Definitions of the modeled parameters.

Parameter	Definition
w	Occupation number of the dominant rotameric state relative to the minor states
k_{rot}	Exchange rate between any two rotameric states defined as a sum of the forward and backward rates
E_{a}	Activation energy of rotameric exchange, $k_{rot} = k_0 e^{-E_a / RT}$
ΔE	Energy difference between the major and minor rotameric states used in the Boltzmann relation, $w = e^{b / R - \Delta E / RT}$
T_1^{eff} and β	Fitting parameters of magnetization decay curves according to the stretched exponential function: $M(t) = M(\infty)(1 - e^{-(t / T_1^{eff})^{\beta}})$
k_{flip}	Flip (exchange) rate between the two orientations of phenylalanine ring (i.e., π -flip)
σ^k	Width of the log-normal distribution of ring-flip rate constants
$\langle E_a^{flip} \rangle$	Average activation energy for π-flips of a phenylalanine ring
σ^{flip}	Standard deviation of the Gaussian distribution of activation energy for π-flips of a phenylalanine ring
p_{bound}	Fraction of the bound state of N-terminal domain residues
D	Effective diffusion coefficient for the fluctuations of free state of the N-terminal domain
k_{ex}	Conformational exchange rate constant between free and bound stat of the N-terminal domain
Tm	Mid-point of the freezing curve
σ	Characteristic width of the transition region of the freezing curves